# Study of a novel microstructured air electrode/electrolyte interface for Solid Oxide Cells

J. F. Basbus[ab]*, D. Cademartori[a], A. M. Asensio[a], D. Clematis[a], L. Savio[c], M. Pani[de], E. Gallus[f], M. P. Carpanese[ab], A. Barbucci[ab], S. Presto[b], M. Viviani[b].

[a] Department of Civil, Chemical and Environmental Engineering (DICCA), University of Genova (UniGe), Via all'Opera Pia 15, 16145 Genoa, GE, Italy.
[b] Institute of Condensed Matter Chemistry and Technologies for Energy (ICMATE), National Research Council (CNR), c/o DICCA-UniGe, Via all'Opera Pia 15, 16145 Genoa, GE, Italy.
[c] Institute of Materials for Electronics and Magnetism (IMEM), CNR, Via Dodecaneso, 33, 16146 Genoa, GE, Italy.
[d] Department of Chemistry and Industrial Chemistry (DCCI), UniGe, Via Dodecaneso, 31, 16146 Genoa, GE, Italy.
[e] Superconducting and other Innovative materials and devices institute (SPIN), CNR, Corso Perrone, 24, 16152 Genoa, GE, Italy.
[f] Kirana S.r.l. – Laser Micromachining, Via Fortunato Zeni, 8, 38068 Rovereto, TN, Italy.

* Corresponding Author: juanfelipe.basbus@edu.unige.it

## Abstract

Solid Oxide Cells (SOCs) are promising high temperature electrochemical devices to obtain clean energies from renewable sources. Their high operating temperatures (800-1000 °C) contribute to the degradation of the cell components. Intermediate Temperature SOCs (IT-SOCs) appear as an alternative to decrease the operating temperatures (600-800 °C) and avoid cell degradation, nevertheless, the electrochemical performance is affected by energy dissipation, principally by the air electrode overpotentials. This work presents the surface modification of $Ce_{0.80}Sm_{0.20}O_{2-\delta}$ (SDC) electrolyte by Femtosecond Laser Micromachining (FLM) to increase the surface/area ratio and therefore improve the electrochemical performance. A pattern with an equally spaced pillar shape microstructure was obtained and characterized. $(La_{0.60}Sr_{0.40})_{0.95}Co_{0.20}Fe_{0.80}O_{3-\delta}$ (LSCF) powder was used as porous air electrode to determine the electrochemical benefits of the pattern. Polarization resistance ($R_p$) of air electrode in patterned sample was about five times lower than in flat one at 600 °C and after 45 h, which suggested an improvement in the electrical and chemical features over time. These enhancements could be explained by the synergistic effect among surface/area ratio, nano-microcrystalline domains and superficial $Ce^{3+}$ concentration in the patterned electrolyte. $R_p$ values are higher than those reported for best air electrodes, however, FLM has proven its benefits in electrochemical performance.

## Keywords

IT-SOCs; pulsed laser patterning; pillar shape microstructure; morphological, chemical and electrical characterization; air electrode/electrolyte interface degradation.

## Highlights

FLM technique was applied to modify the surface of an IT-SOC electrolyte.

Patterned SDC electrolyte presented a well-spaced and distributed pillar shape microstructure.
Different grain size, high surface/area ratio and mixed oxidation states were detected.
Pillar shape microstructure improved electrical and chemical performance over time.
A correlation between microstructure and superficial mixed oxidation states is proposed.

## Introduction

The global demand of electricity and fossil fuels is constantly increasing while the energetic policies aim at achieving net zero greenhouse gas emissions in the next decades. All of these reasons encourage the development of new technologies to obtain clean energies from renewable sources and improve circular economy of fuels [1,2]. In this sense, electrochemical cells are gaining more and more attention due to their capability to transform chemical energy into electrical energy and vice versa with high efficiency and low environmental impact [3,4]. Particularly, Solid Oxide Cells (SOCs) are the most promising due to: i) favorable kinetics, ii) no use of Platinum Group Metal elements, iii) high tolerance to medium and low quality fuels, and iv) suitability for combined heat and power generation [5]. Despite the great breakthrough made in recent years, improvements in SOCs durability are still required [6]. Decreasing operating temperature below 800 ºC remains crucial to control cells and stacks degradation [7]. On the other hand, these low temperatures imply a decay of the overall efficiency due to the higher electrode overpotentials and lower electrolyte conductivity. State-of-the-Art (SoA) strategies to reduce operating temperature and costs, and to increase their durability mainly rely on: i) reducing the thickness of the electrolyte to values below 10 μm; ii) exploring the use of materials with higher ionic conductivity at lower temperature compared to commonly used electrolyte materials, such as yttria-stabilized zirconia (YSZ) and (Ce,Y,Gd,Sm)$O_{2-\delta}$ solid solutions; and iii) designing new microstructures and architectures to improve the electrochemical performance [8,9]. Particularly, doped ceria electrolytes have been proposed due to the fact that operate at Intermediate Temperature (IT) range, i.e., 600-800 °C [10,11]. Mathematical simulations explored possible advantages coming from having an array of pillars on the surface of SOC electrolyte, both from the point of view of increasing the interface area and of enhancing ionic conduction pathways inside the electrodes. Depending on the activity of materials and on the shape/size of pillars, an increase of the current density up to 30-40 % can be expected [12,13]. Indeed, several advanced processing techniques have been successfully employed to introduce mesoscale patterning of the electrolyte surface, including laser patterning, impregnation of microporous scaffolds, freeze tape casting, metal mesh pressing, soft-lithography, ultraviolet nanoimprint lithography and inkjet printing. These techniques have been applied to SOCs electrolytes leading to improved thermomechanical properties and performance [14–19]. Particularly, Femtosecond Laser Micromachining (FLM) allows to machine a broad range of materials with very high accuracy due to the reduced heat affected zone as well as lower micro-cracks and surface deposited debris. Additionally, FLM ultimately requires few post-processing operations, typically composed by an ultrasonic bath [20]. Such features make FLM an ideal candidate for the direct machining of ceramic materials. This technique was applied to create holes in metallic/ceramic composites, drilled holes in composite/cermet, hexagonal arrangements, etc. [21,22]. Several works indicate a significant improvement of the activity of the electrode/electrolyte interface in electrolyte-supported cells. For example, Cebollero et al. performed an intensive study of YSZ patterned electrolyte for SOCs applications and determined the electrochemical properties in composite based on lanthanum strontium

manganate/YSZ (LSM-YSZ) electrodes [14,23,24]. They observed a reduction up to 40 % in the polarization resistance ($R_p$) at 800 °C, related to the increased interface area (130 %) and partially hindered by the spread of triple-phase boundary area across the electrode volume. The interaction of a laser beam with YSZ surface also resulted in the formation of a thin nanostructured layer with the same composition of the electrolyte, due to condensation of the vapor formed from the ablation plasma [23]. Alternatively, Cai et al. realized a periodic pattern of dimples by FLM (area increased by 39 %) on both the anodic and the cathodic side of a YSZ electrolyte before sintering, observing a 51 and 33 % decrease of the ohmic and total $R_p$, respectively, in a complete cell with state-of-the-art electrodes (LSM-YSZ cathode, Ni-YSZ anode) at 800 °C [25]. Zheng et al. reported a multi-physical field modeling and concavo-convex electrolyte surface modification by printing technology, showing better performance than planar cell but without substantial improvements of the degradation rate under constant current [26]. Such results should encourage the design of microstructured cells, especially when aiming at the development of SOCs operating at lower temperatures.

In this work, the surface modification on an IT-SOC electrolyte and its effect on the $R_p$ of the air electrode is reported. $Ce_{0.80}Sm_{0.20}O_{2-\delta}$ (SDC) electrolyte was modified by FLM technique and, microstructural and electrochemical characterization were done. $(La_{0.60}Sr_{0.40})_{0.95}Co_{0.20}Fe_{0.80}O_{3-\delta}$ (LSCF) perovskite was selected as air electrode due its well-known electrochemical performance and good mixed electronic-ionic conductivity [27]. Electrolyte-electrode interface during a short period was studied and compared with a standard flat sample to evidence improvements related to the laser machining.

## Experimental

### *Dense electrolyte preparation and patterning*

High purity SDC powders (> 99.99 %) from Fuelcellmaterials company were used for the preparation of the electrolytes. These were uniaxially pressed as pellets without any binder at 60 MPa (using a 25.4 mm die) and then sintered at 1450 °C in air for 4 hours. Then, SDC sintered pellets were patterned on one face by a femtosecond laser system Pharos PH1 Light Conversion, emitting pulses of 214 fs on the fundamental wavelength of 1030 nm. The laser beam was focused by a 100 mm F-Theta lens and scanned across the sample by ExcelliScan SCANLAB galvanometric scanners. Pillar shape microstructure was developed over a circular area of 6 mm diameter through layer-by-layer removal in air at room temperature (RT).

### *Structural and morphological study of dense electrolyte*

White Light Interferometry (WLI) was used to verify the overall pillar shape in air at RT by using SmartWLI GBS equipment. The microstructure of SDC dense pellets was observed by Scanning Electron Microscopy (SEM) using a Phenom ProX equipment, coupled with Energy Dispersive Spectroscopy (EDS) for elemental analysis, operated a 15 kV in ultra-high vacuum, with an accuracy better than 1 %, energy resolution above 0.01 keV and atomic-number, absorption and fluorescence (ZAF) correction. Point analysis as well as elemental mapping were performed.

Crystallographic properties of patterned samples were evaluated by X-Ray Diffraction (XRD) at RT in air. For this purpose, it was used a PANalytical AERIS equipment operated at 30 kV and 10 mA, with Bragg-Brentano geometry, Cu $K_\alpha$ radiation, angular range (2θ) of 20-90 °, 0.011 ° step size, Ni filter and PIXcel$^{1D}$ detector. In addition, the

profiles of both flat and patterned electrolytes were refined by the Rietveld method using the Fullprof Suite. A 6$^{th}$ degree polynomial, Thompson–Cox–Hastings pseudo-Voigt convoluted with axial divergence asymmetry function and isotropic Debye–Waller factors were used for background fit, peak profiles and atomic thermal displacement, respectively. *Fm-3m* (N° 225) space group was used as seed, Wyckoff positions (WP) for (Ce,Sm) and O were assigned as 4a, and 8c, respectively.
The same samples were analyzed by X-ray Photoelectron Spectroscopy (XPS) after laser patterning to verify the oxidation state of the elements on the surface. The measurements were performed in an ultra-high vacuum chamber with base pressure better than $5x10^{-8}$ mbar. XPS spectra were recorded using a hemispherical analyzer model 10–360 and a monochromatic Al $K_\alpha$ X-ray source model 10–610 by Physical Electronics. An electron gun was employed for charge neutralization during the measurement of the insulating sample. Photoemitted electrons were collected from a spot of approximately 100 μm diameter, so that it was possible to both analyze non-treated and patterned areas from the same sample. XPS spectra were analyzed using the KolXPS software. Binding Energies (BEs) were calibrated by setting the maximum of the C 1s line to 284.5 eV [28]. All regions were fitted using Voigt functions and a Shirley background. Up to three and four components were used to fit the C 1s and O 1s traces, respectively, while two doublets were necessary to reproduce the Sm 3d region. The Ce 3d spectrum is definitely more complex since it consists of four doublets taking into account the presence of atoms in both $Ce^{4+}$ and $Ce^{3+}$ oxidation state. At the end of the fitting procedure, the fitted background is subtracted to the spectra for a better visualization.

*Preparation of electrodes on electrolyte samples and three-electrodes set-up*

Electrodes for electrochemical testing in air were made of LSCF and deposited by slurry coating. The ink was prepared by mixing in an agate mortar pure LSCF powders (> 99.9 %, Fuelcellmaterials) and α-terpineol (> 96%, SAFC) in a mass ratio of 30 and 70 %, respectively. The ink was deposited on both faces of the supporting SDC electrolyte pellet: in the center of each side as 6 mm diameter disks to operate as working (on the patterned area) and counter electrode, respectively. A third electrode (reference electrode) was shaped as a ring around the patterned area, with a suitable geometry to avoid artefacts during the Electrochemical Impedance Spectroscopy (EIS) measurements [29].
The three electrodes were prepared at the same moment. After ink layers deposition, α-terpineol was evaporated in a vacuum (47 Pa) at RT. The electrodes were thermally treated at 1100 °C in air for 2 hours. The same procedure was adopted for samples without patterning, to be tested for comparison sake.

*Electrochemical testing and post–test analyses*

The electrical properties of three-electrodes cells were evaluated by EIS. The measurements were performed in a commercial rig (ProboStat, Norecs) coupled with an impedance and electrochemical meter (IviumSTAT-N, IVIUM). The spectra were recorded as a function of time (t) for 48 hours, in the frequency range from $1x10^6$ to 0.1 Hz with 50 mV amplitude, under pure $O_2$ flow (50 $mlmin^{-1}$) at 600 °C. Platinum mesh and wires were used as current collectors. EIS data were analyzed by the Extended Domain Distribution of Relaxation Times (ED-DRT) method for the electrochemical data deconvolution [30].

SEM was used to determine the electrode microstructure after electrochemical measurements. In the same way, XRD was used to compare crystallographic properties before and after electrochemical testing.

## Results and Discussion

*Characterization of the patterned electrolyte*

Previous simulations suggested the possibility to improve the performance of electrodes by realizing a pattern of pillars 20-35 µm wide, 20-30 µm tall and spaced 40-80 µm from each other [12,13]. Such structures can be suitably obtained by FLM with sufficient accuracy and speed [31,32]. A step (d) of 80 µm among the pillars was selected to ensure a suitable spacing to deposit electrode paste with good reproducibility, as well as height (h) of 22 µm. Figure 1 shows WLI analysis of the SDC patterned sample where it can be observed a quite uniform distribution and equally spaced truncated-conic profile of the pillars, with base and top diameter of about 44 and 16 µm, respectively.
The increase of the surface area caused by patterning, was evaluated by adding the area increment of each pillar ($\delta S_i$) to the area of a flat surface ($S_0$). Assuming an ideal truncated-cone shape for each pillar, the area increment is given by $\delta S_i = S_l + \pi(r_1^2 - r_2^2)$, where $r_1$ and $r_2$ are the top and base surface radii, respectively. The lateral surface of a pillar ($S_l$) is expressed by $S_l = \pi(r_1 + r_2)\sqrt{h^2 + (r_2 - r_1)^2}$. In this sense, the area increment factor ($K_s$) can be calculated as $K_S = \frac{S}{S_0} = \frac{S_0 + N\delta S_i}{S_0} = 1 + \frac{N\delta S_i}{\pi r^2}$, with $r_1$ = 8 µm and $r_2$ = h = 22 µm meanwhile r = 3000 µm and N = 4420 correspond to the radius and the number of pillars within the patterned area, respectively. In this case, $K_s$ is about 1.46.

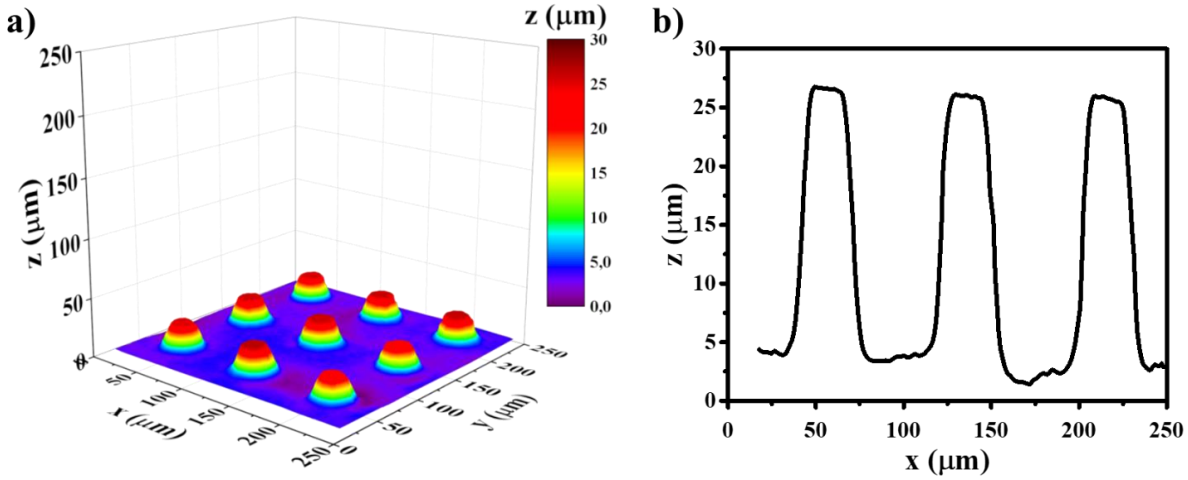


**Figure 1.** a) WLI plot and b) profile cut along the horizontal direction. Note the expanded scale on z axis. These images correspond to SDC patterned sample realized by FLM.

Figure 2 indicates, the shape and distribution of the pillars on SDC pellet. In addition to the area increment, a superficial effect of the laser ablation on microstructure was observed. The SEM image of one pillar in the patterned area, reported in Figure 3a, clearly shows the difference between laser patterned and as-sintered surfaces. It shows a conserved grain sizes in the top of the pillar (i.e., center of the image), meanwhile, the laser ablated area presents a porous layer with grains and voids of about 200–400 nm.

EDS point analysis also revealed higher oxygen deficiency of patterned surface with respect to as-sintered. The O atomic content in the reference sample was around 66 % in agreement with the stoichiometric ratio, meanwhile in patterned sample it was below 50 % which suggests $Ce^{4+}$ reduction in the surface (see Table 1). These findings could be explained by a local melting induced by laser power absorption, followed by condensation and recrystallization possibly implying partial reduction of the material. XRD evidenced a broadening of SDC peaks in patterned areas with respect to as-sintered ones, while no significant peak shifts were observed. Figure 4a shows the comparison at high angles where the difference is evident, while the full pattern is presented in Figure 4b. In both cases, the refinements indicated a quite similar lattice parameter (a), profile factor ($R_p$), weighted profile factor ($R_{wp}$) and chi-square ($\chi^2$) values [33,34]. In particular, the patterned sample indicates a = 5.4345(1) Å, $R_p$ = 7.45 %, $R_{wp}$ = 9.92 % and $\chi^2$ = 3.31 %. Crystallite size (CS) was estimated around 63 nm by using the flat sample as standard due its large grain sizes (i.e., 5 µm), peaks with narrow full width at half maximum (FWHM) and equal 2θ positions. Although this can be considered an underestimation of the real value, due to the contribution to diffracted intensity from original grains located below the surface (Bragg Brentano geometry and X-ray penetration length) and on top of pillars, it is in good agreement with above mentioned SEM images. In order to check the possible effect of laser ablation on the oxidation state, XPS analyses were carried out both on as-sintered and patterned areas. Figure 5 compares XPS spectra of the Ce 3d and O 1s regions acquired on the flat (bottom panels) and micropatterned (top panels) areas of the sample. The corresponding Sm 3d and C 1s regions are reported and discussed in Figure A.1 of Appendix A for completeness.

Microstructuring significantly affects the Ce 3d region (see Figure 5a) and reveals a significant increase of the $Ce^{3+}$ concentration in the patterned area. Ce 3d spectra are in perfect agreement with those reported in literature: they present the three doublets with BE(Ce $3d_{5/2}$) at 881.1, 887.7 and 897.4 eV, which are typical of $Ce^{4+}$ [35,36]. In addition, a fourth doublet with BE(Ce $3d_{5/2}$) = 885.5 eV, indicative of the presence of $Ce^{3+}$ [36], is observed as a minor component in the spectrum of the flat area, and increases by a factor of three for the patterned sample. Indeed, the area of the $Ce^{3+}$ and $Ce^{4+}$ lines is estimated to be, respectively, ~ 3.5 and 96.5 % of the total Ce 3d intensity for the flat sample; these values change into ~ 11.5 and 88.5 % for the patterned sample. Since photoemission from $Ce^{3+}$ or $Ce^{4+}$ occurs with the same cross section and photoelectrons have very close kinetic energy (i.e., same escape depth), the relative amount of the two Ce species in terms of atomic % scales directly with their area ratio, admitting a uniform distribution of the $Ce^{3+}$ ions within the probed surface layers.

The O 1s region of the flat area shows two peaks (see Figure 5b), which can be resolved in three lines. The major peak is located at 528.4 eV and is due to lattice $O^{2-}$ bounded to $Ce^{4+}$ and $Sm^{3+}$, while the lines at 530.9 eV and 532.0 eV originate from adsorbed $OH^-$ groups and, possibly, undissociated water molecules. It is indeed well established for all oxides that the 531-532 eV signals can be related to vacancy formation, that are soon saturated by water/hydroxide groups [37]. Although a BE close to 532.0 eV has also been identified with $O^{2-}$ in defective (oxygen-deficient) environment [36,38], the former assignment is more reasonable since the sample was kept in air before XPS analysis.

**Table 1.** Elemental composition (at. %) by EDS point analysis on both surfaces.

| Atom | non-treated | patterned |
|---|---|---|
| **Ce** | 27 | 39 |
| **Sm** | 9 | 13 |
| **O** | 64 | 48 |

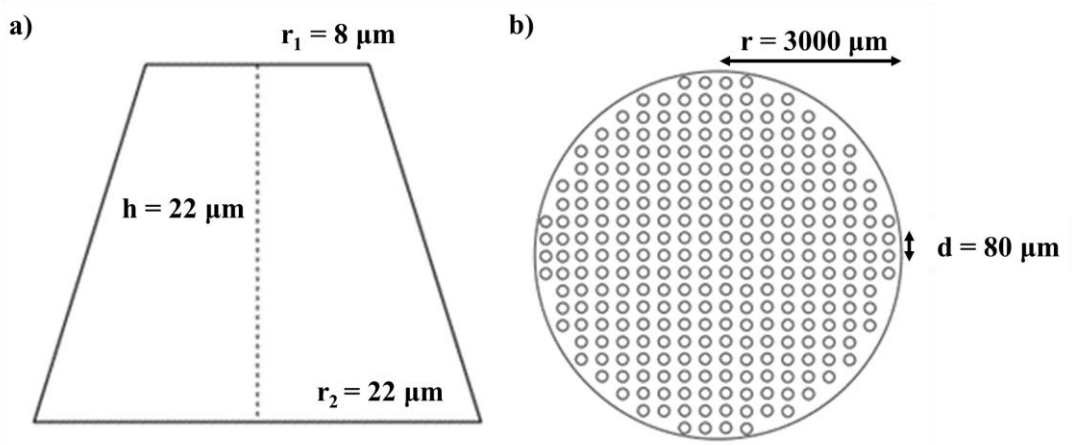


**Figure 2.** Schematic of pattern realized by FLM. a) Side view of a pillar and b) top view of patterned area.

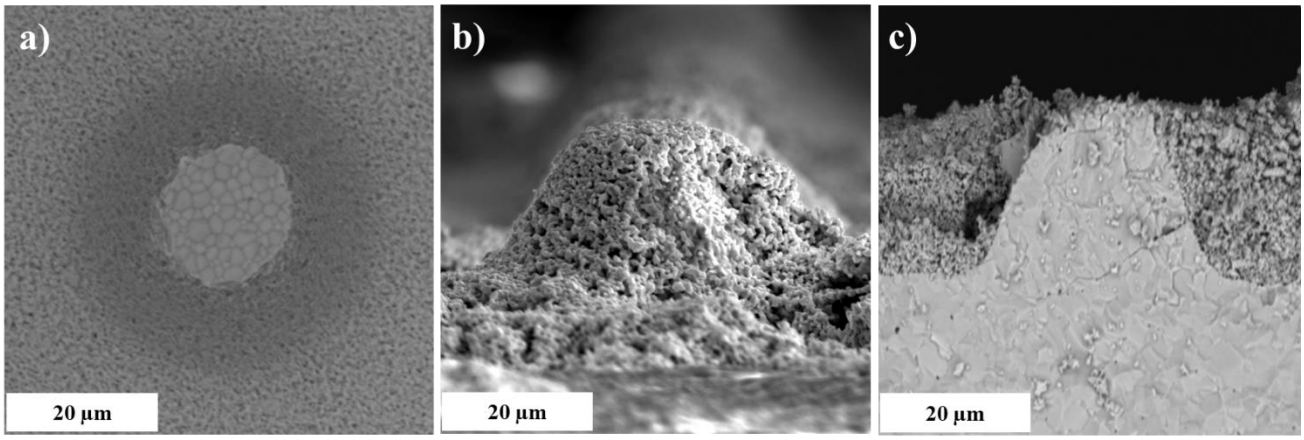


**Figure 3.** SEM images of the a) top view of patterned SDC surface, b) SDC pillar covered with LSCF and c) its cross section.

The spectrum of the patterned area shows a decrease of absorbed $OH^-$ species at BE = 530.9 eV and of the oxygen signal at regular sites (also upshifting to BE = 528.8 eV). Simultaneously, a new line appears at 527.7 eV, that could be assigned to an additional oxygen species related to increased surface disorder. We observe that the amount of adsorbed species at the surface is determined by several factors, including sample handling, but lattice oxygen can be considered as an indirect measure of oxygen vacancies concentration [39]. It is evident that the nanopatterned sample presents a reduction of those peaks related to the presence of oxygen or adsorbates at regular sites, that is compensated by the increase in intensity of lines corresponding to a defective/disordered environment [37,38]. This behavior agrees with that of the $Ce^{3+}$ component in the Ce 3d regions and with the one observed by EDS thus suggesting an increase of the oxygen vacancy concentration caused by laser patterning.

Therefore, XPS suggests that the increased $Ce^{3+}$ content in the patterned area is related to the local formation of oxygen vacancies and/or electron-hole concentration with respect to the untreated area. In this sense, the laser patterning not only accurately modifies the microstructure, but it also affects the oxidation states. In turn, these changes could modify the electrode-electrolyte interface and electrochemical performance.

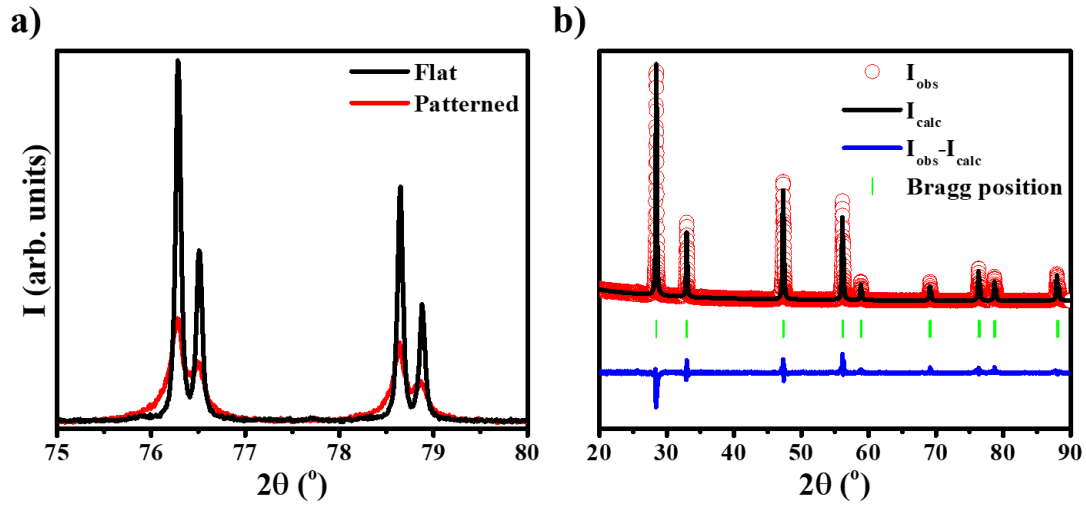


**Figure 4.** a) Comparison between XRD patterns for flat and patterned samples in air at RT. The intensity (I) is expressed in arbitrary units. b) Rietveld refinement for patterned sample. Observed I ($I_{obs}$), calculated I ($I_{calc}$), difference between both ($I_{obs}$-$I_{calc}$), and Bragg positions are indicated.

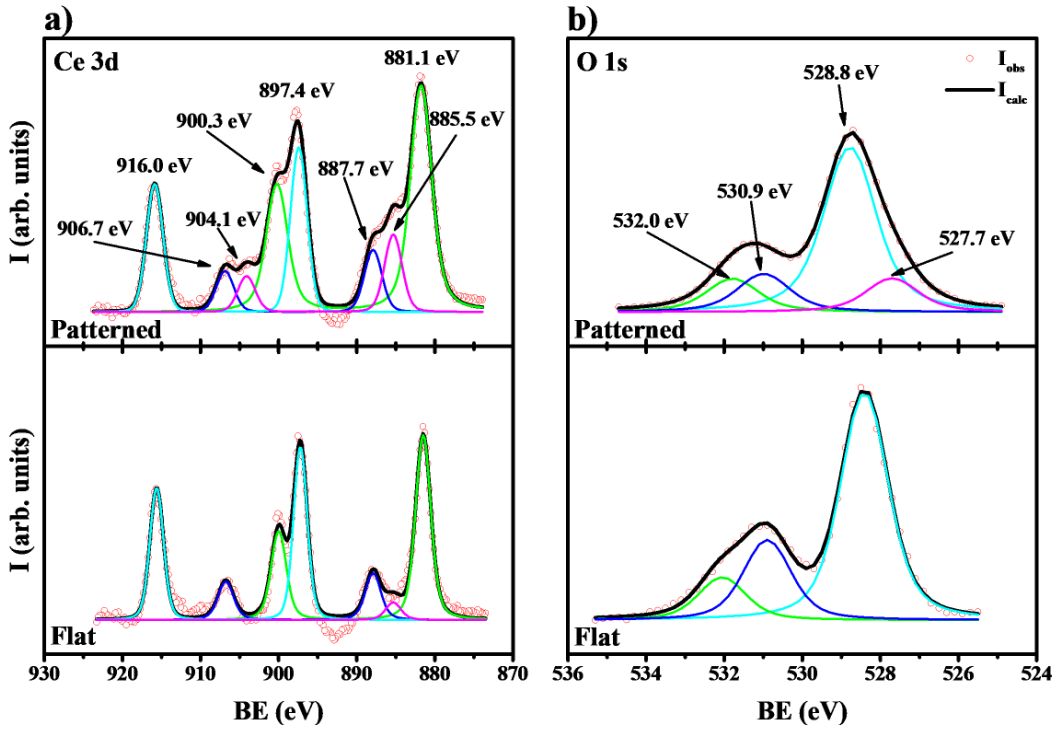


**Figure 5.** XPS analysis on patterned (top panels) and flat (bottom panels) samples. Comparison of a) Ce 3d and b) O 1s regions. Colored lines (i.e., green, blue, cyan and magenta) correspond to the individual contribution of each peak to the overall profile fitting. The BE of each peak is also indicated.

*Chemical and electrical characterization of three electrodes configuration cell*

SEM images of cells after electrode ink deposition and thermal treatment shows good adhesion between LSCF electrode and SDC electrolyte (Figure 3b and c). Porosity of electrode layer is homogeneous in both patterned and flat interfaces. The electrochemical

performance of the three electrodes cells was analyzed by EIS. Figure 6a compares the Nyquist plot of a patterned sample with that of a flat standard cell, both collected at 600 °C under pure $O_2$ flow. The $R_p$ was calculated by the difference between the intersections of the plot with real axis (Z´). In this sense, $R_p$ of the flat cell was equal to 1.59 $\Omega cm^2$, while that of the machined sample was reduced to 1/4 of it (i.e., 0.40 $\Omega cm^2$). Further details can be obtained by the ED-DRT analysis indicated in Figure 6b, which compares both samples at 600 °C as a function of time. At initial time (i.e., t = 0 h), the flat sample evidenced three characteristic frequencies, and the main peak is observed in the range of 1-10 Hz. This contribution drastically decreased in the patterned sample, that has a spectrum showing two contributions, with the most relevant at intermediate frequency (i.e., around 100 Hz). The observed decrease in peak area and its shifting at higher frequencies in the patterned sampled could be related to the increased surface area available for the reaction, which improves the kinetic of oxygen reduction.

It is evident that the introduction of the pillars has a high impact on lower frequency processes, that in the literature has been attributed to gas diffusion or to the oxygen reduction reaction at cathode surface [40–42]. Considering that the EIS measurements have been carried out using a pure oxygen flow, it could be reasonable to neglect issues related with diffusion in the gas phase, and then link this process with the surface reaction. This hypothesis is supported also by the DRT curves from EIS, that highlight how the thermal ageing mainly affects the low frequency arc (see Figures 6b). Figure 6c presents the evolution and overall effect of aging test. The $R_p$ of both samples increased almost linearly with time up to 45 hours, even though with quite a different rate. However, ohmic resistance ($R_{ohm}$) of SDC electrolytes for both samples did not show significant changes (3.1 and 2.9 $\Omega cm^2$ for patterned and flat sample, respectively) until 45 hours. In particular, the degradation rate in cells with patterned electrolyte was about five times lower than in flat samples. It should be considered that aging is usually quicker at early stages than after thousands of hours of operation [43,44]. Similar degradation rates were obtained at 650 °C for pure LSCF and mixed LSCF-BSCF electrodes on SDC electrolyte [45,46]. A strong performance degradation at 550 °C in Ni-SDC/SDC/LSCF-SDC cell was related to the diffusion of La into the electrolyte, Ce/Sm into the electrode and $SrCO_3$ formation [35]. Fuel and electrolysis cells under operation conditions suffered significant effects at the interfaces, Sr segregation and diffusion [47,48]. In this work, SrO formation is expected due to pure oxygen atmosphere during the EIS measurements in LSFC/SDC samples. However, it must be noted that, despite the larger area, the degradation was slower in patterned cells than in flat ones. A possible explanation considers the microstructure at the interface, made of fine grains and pores of about same size and homogenously distributed. The diffusion path for Sr can be through bulk or grain boundaries, depending on local physical-chemical conditions. Different grain sizes may affect the process by modifying the relative grain boundary concentration. Under this hypothesis, the different degradation ratios observed here might be therefore attributed to the different microstructure. Further confirmation comes from XRD analysis from cells. XRD patterns of LSCF/SDC powders mixture of equal mass ratio (i.e., 50 % of mass ratio) did not evidence a change before and after thermal treatment at 1100 °C in air. It has been reported pores formation and delamination processes for LSFC air electrodes in SOCs [49]. However, XRD patterns of cells showed some differences in Bragg reflections of LSCF between pristine and aged samples, possibly due to the composition changes at the interface related to Sr diffusion (see Figure 6d). In the same way, EDS mapping of the patterned cell after EIS measurements supports Sr diffusion hypothesis (see Figure 7). Point analysis indicates an atomic concentration around 5 % of Sr into the pillars, meanwhile La, Co and Fe were about 1 %, discarding their diffusion into the electrolyte,

as well as Ce and Sm into the electrode. In addition, O content into the fluorite electrolyte is slightly higher than perovskite electrode, which it agrees with their structure. Patterning improved electrical and chemical performance over time with respect to a flat sample, thanks to surface microstructure reorganization and $Ce^{3+}$ formation. Although the reported values of $R_p$ are not comparable with SoA materials, results are indicative of the improvements that can be obtained by applying FLM to ceramic interfaces.

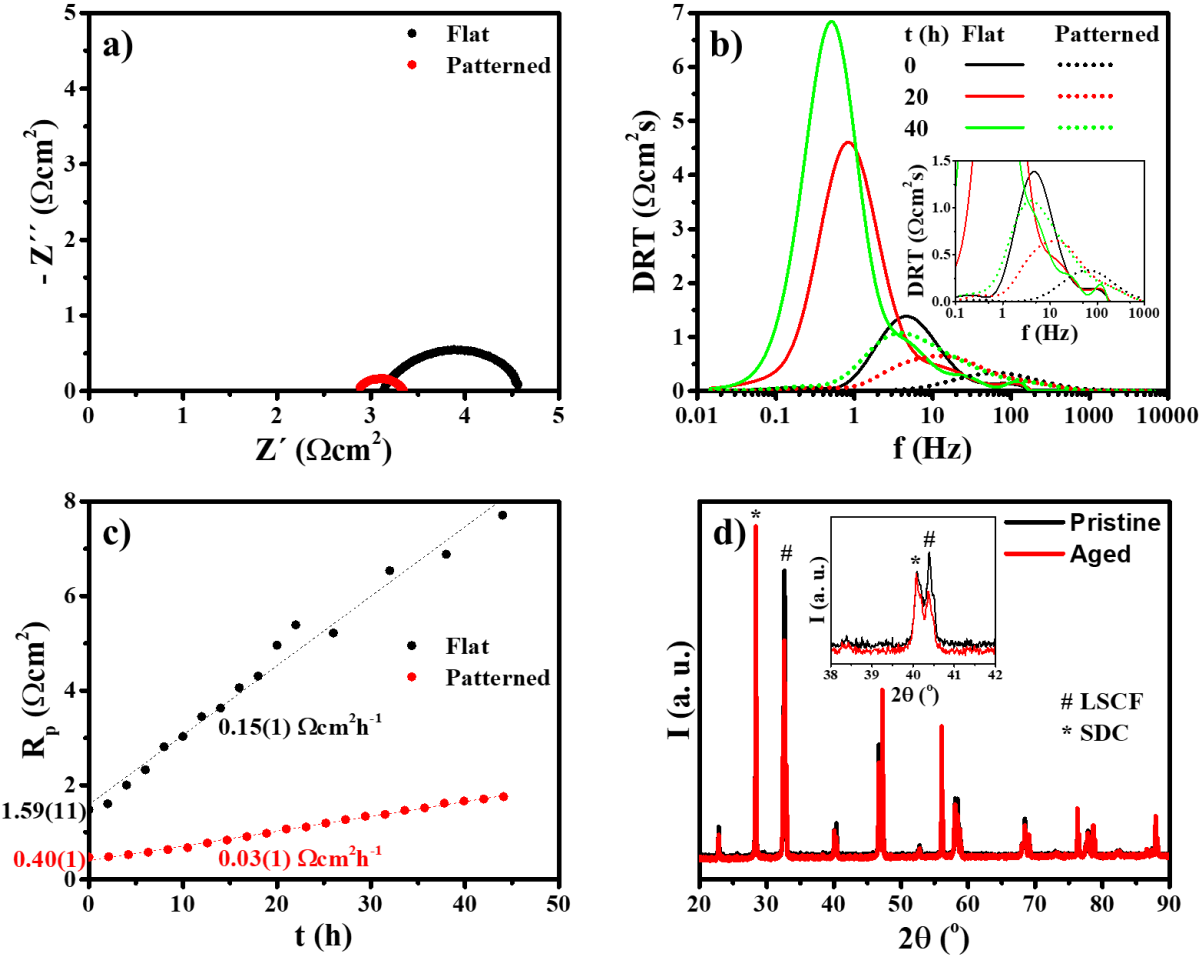


**Figure 6.** a) Nyquist plot at initial conditions. b) DRT profiles and c) $R_p$ as a function of time. d) XRD profiles of patterned sample before and after testing.

## Conclusions

FLM was applied to fabricate pillar shaped microstructure on SDC electrolyte to verify the performance improvement indicated by simulations. The SDC patterned sample presented a quite uniform distribution and equally spaced truncated-conic profile. In addition, femtosecond laser ablation produced a fine-grained microstructure and increased the concentration of $Ce^{3+}$ ions in association with oxygen vacancies. Symmetrical SOC cells realized by adding LSCF air electrodes showed a significant reduction of the polarization resistance with respect to standard flat cells, exceeding the area increment factor. Possible positive synergistic effect on the charge transfer process can be ascribed to the higher concentration of oxygen vacancies at the surface of patterned electrolytes. Degradation of performance was observed and correlated to migration of cations across the electrode/electrolyte interface, partially hindered by the fine-grained

microstructure obtained after laser machining. Electrolyte patterning by FLM technique allows it to decrease the resistance of air electrode and to increase the lifetime in a cell.

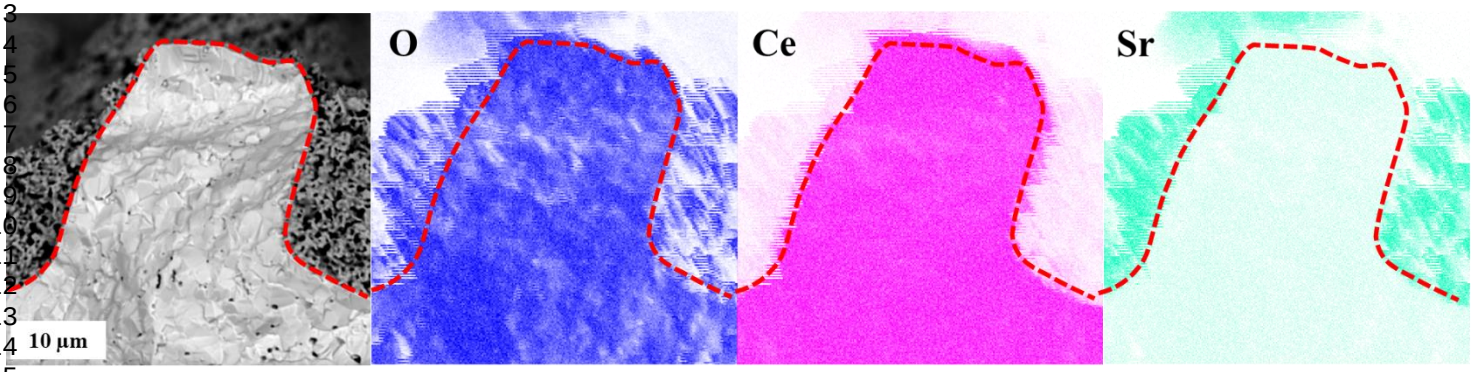


**Figure 7.** EDS mapping of the patterned cell after EIS testing. Red dashed line outlines the LSCF and SDC regions.

## Appendix

Figure A.1 shows the XPS spectra of the Sm 3d and C1s regions measured for the flat (bottom panels) and micro-patterned (top panels) areas of the sample. The Sm 3d region does not show significant changes between patterned and flat area, since both XPS spectra can be fitted with two Voigt doublets of identical shape and BE (Sm $3d_{5/2}$) at 1078.0 and 1082.0 eV, respectively. The higher BE peak can be assigned to $Sm^{3+}$, while the smaller component is due to the charge transfer effect of the unpaired 4f electrons [36]. The C 1s region of the flat area shows a large signal at 284.5 eV, typical of adventitious carbon, while a secondary line at 288.4 eV is related to carbonate/carbonyl/carboxyl groups, indicative of some organic contamination of the sample. In the patterned area, the main peak gets lower, larger and asymmetric, since a new component grows at low BE, while the overall amount of C reduces. This suggests that the laser power induces partial cleaning of the surface together with the conversion of part of the C contaminants in carbonaceous/carbide species [50].

## CRediT authorship contribution statement

**J. F: Basbus**: Conceptualization, Investigation, Formal analysis, Visualization, Writing – original draft, Writing – review & editing. **D. Cademartori**: Investigation, Writing – original draft. **A. M. Asensio**: Investigation, Writing – original draft. **D. Clematis**: Formal analysis, Writing – original draft. **L. Savio**: Investigation, Formal analysis, Visualization, Writing – original draft. **M. Pani**: Conceptualization, Writing – original draft. **E. Gallus**: Investigation, Writing – original draft. **M. P. Carpanese**: Conceptualization, Writing – original draft. **A. Barbucci**: Conceptualization, Writing – original draft. **S. Presto**: Conceptualization, Investigation, Visualization, Writing – original draft. **M. Viviani**: Conceptualization, Investigation, Formal analysis, Visualization, Writing – original draft.

## Declaration of Competing Interest

The authors declare that they have no known competing financial interests or personal relationships that could have appeared to influence the work reported in this paper.

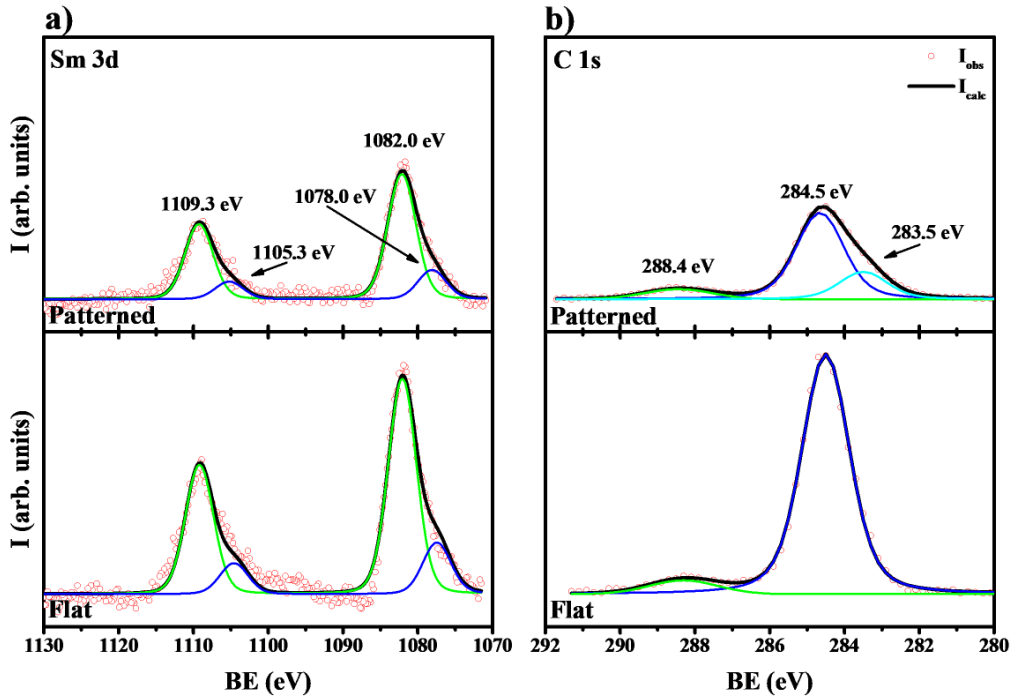


**Figure A.1.** Idem to Figure 5, comparison between a) Sm 3d and b) C 1s regions for patterned and flat samples.


## Acknowledgements

This work was carried out in the frame of the projects "Production of renewable fuel by CO-ELectrolysis and reUSe of carbon dioxide (COELUS)" and "MC-nano", supported by Fondazione Compagnia di San Paolo. In addition, it was supported by "Network 4 Energy Sustainable Transition (NEST) under "National Recovery and Resilience Plan (PNRR)". We also thank F. Bassi and M. Verdi from Kirana S.r.l. – Laser Micromachining for their support during sample preparation.


## References


[1] J.O. Abe, A.P.I. Popoola, E. Ajenifuja, O.M. Popoola, Hydrogen energy, economy and storage: Review and recommendation, Int. J. Hydrogen Energy. 44 (2019) 15072–15086. https://doi.org/10.1016/j.ijhydene.2019.04.068.

[2] N. Sazali, Emerging technologies by hydrogen: A review, Int. J. Hydrogen Energy. 45 (2020) 18753–18771. https://doi.org/10.1016/j.ijhydene.2020.05.021.

[3] D. Akinyele, E. Olabode, A. Amole, Review of Fuel Cell Technologies and Applications for Sustainable Microgrid Systems, Inventions. 5 (2020) 42. https://doi.org/10.3390/inventions5030042.

[4] Y. Zheng, Z. Chen, J. Zhang, Solid Oxide Electrolysis of H2O and CO2 to Produce Hydrogen and Low-Carbon Fuels, Electrochem. Energy Rev. 4 (2021) 508–517. https://doi.org/10.1007/s41918-021-00097-4.

[5] A. Hauch, R. Küngas, P. Blennow, A.B. Hansen, J.B. Hansen, B. V. Mathiesen, M.B. Mogensen, Recent advances in solid oxide cell technology for electrolysis, Science (80-. ). 370 (2020). https://doi.org/10.1126/science.aba6118.

[6] J. Zhu, Z. Lin, Degradations of the electrochemical performance of solid oxide fuel cell induced by material microstructure evolutions, Appl. Energy. 231 (2018)

22–28. https://doi.org/10.1016/j.apenergy.2018.09.127.
[7] J. Zamudio-García, L. Caizán-Juanarena, J.M. Porras-Vázquez, E.R. Losilla, D. Marrero-López, A review on recent advances and trends in symmetrical electrodes for solid oxide cells, J. Power Sources. 520 (2022) 230852. https://doi.org/10.1016/j.jpowsour.2021.230852.
[8] T. Mori, R. Wepf, S.P. Jiang, Future prospects for the design of 'state-of-the-art' solid oxide fuel cells, J. Phys. Energy. 2 (2020) 031001. https://doi.org/10.1088/2515-7655/ab8f05.
[9] A. Nechache, S. Hody, Alternative and innovative solid oxide electrolysis cell materials: A short review, Renew. Sustain. Energy Rev. 149 (2021) 111322. https://doi.org/10.1016/j.rser.2021.111322.
[10] S. Anirban, A. Dutta, Revisiting ionic conductivity of rare earth doped ceria: Dependency on different factors, Int. J. Hydrogen Energy. 45 (2020) 25139–25166. https://doi.org/10.1016/j.ijhydene.2020.06.119.
[11] M.K. Hossain, G.A. Raihan, M.A. Akbar, M.H. Kabir Rubel, M.H. Ahmed, M.I. Khan, S. Hossain, S.K. Sen, M.I.E. Jalal, A. El-Denglawey, Current Applications and Future Potential of Rare Earth Oxides in Sustainable Nuclear, Radiation, and Energy Devices: A Review, ACS Appl. Electron. Mater. 4 (2022) 3327–3353. https://doi.org/10.1021/acsaelm.2c00069.
[12] F. Delloro, M. Viviani, Simulation study about the geometry of electrode-electrolyte contact in a SOFC, J. Electroceramics. 29 (2012) 216–224. https://doi.org/10.1007/s10832-012-9766-8.
[13] A. Bertei, F. Tariq, V. Yufit, E. Ruiz-Trejo, N.P. Brandon, Guidelines for the Rational Design and Engineering of 3D Manufactured Solid Oxide Fuel Cell Composite Electrodes, J. Electrochem. Soc. 164 (2017) F89–F98. https://doi.org/10.1149/2.0501702jes.
[14] J.A. Cebollero, R. Lahoz, M.A. Laguna-Bercero, A. Larrea, Tailoring the electrode-electrolyte interface of Solid Oxide Fuel Cells (SOFC) by laser micro-patterning to improve their electrochemical performance, J. Power Sources. 360 (2017) 336–344. https://doi.org/10.1016/j.jpowsour.2017.05.106.
[15] Y. Du, N. Hedayat, D. Panthi, H. Ilkhani, B.J. Emley, T. Woodson, Freeze-casting for the fabrication of solid oxide fuel cells: A review, Materialia. 1 (2018) 198–210. https://doi.org/10.1016/j.mtla.2018.07.005.
[16] C. Timurkutluk, T. Altan, F. Yildirim, S. Onbilgin, M. Yagiz, B. Timurkutluk, Improving the electrochemical performance of solid oxide fuel cells by surface patterning of the electrolyte, J. Power Sources. 512 (2021) 230489. https://doi.org/10.1016/j.jpowsour.2021.230489.
[17] C. Lee, S.S. Shin, J. Choi, J. Kim, J.-W. Son, M. Choi, H.H. Shin, A micro-patterned electrode/electrolyte interface fabricated by soft-lithography for facile oxygen reduction in solid oxide fuel cells, J. Mater. Chem. A. 8 (2020) 16534–16541. https://doi.org/10.1039/D0TA03997G.
[18] R. Akama, T. Okabe, K. Sato, Y. Inaba, N. Shikazono, A. Sciazko, J. Taniguchi, Fabrication of a micropatterned composite electrode for solid oxide fuel cells via ultraviolet nanoimprint lithography, Microelectron. Eng. 225 (2020) 111277. https://doi.org/10.1016/j.mee.2020.111277.
[19] N.M. Farandos, L. Kleiminger, T. Li, A. Hankin, G.H. Kelsall, Three-dimensional Inkjet Printed Solid Oxide Electrochemical Reactors. I. Yttria-stabilized Zirconia Electrolyte, Electrochim. Acta. 213 (2016) 324–331. https://doi.org/10.1016/j.electacta.2016.07.103.
[20] N. Faisal, D. Zindani, K. Kumar, S. Bhowmik, Laser Micromachining of

Engineering Materials—A Review, in: 2019: pp. 121–136. https://doi.org/10.1007/978-3-319-99900-5_6.
[21] A. Morán-Ruiz, K. Vidal, A. Larrañaga, R. Montero, M.I. Arriortua, Femtosecond laser micromachining of metallic/ceramic composite material for solid oxide fuel cell devices, Int. J. Hydrogen Energy. 41 (2016) 17053–17063. https://doi.org/10.1016/j.ijhydene.2016.07.122.
[22] R.I. Merino, M.A. Laguna-Bercero, R. Lahoz, Á. Larrea, P.B. Oliete, A. Orera, J.I. Peña, M.L. Sanjuán, D. Sola, Laser processing of ceramic materials for electrochemical and high temperature energy applications, Boletín La Soc. Española Cerámica y Vidr. 61 (2022) S19–S39. https://doi.org/10.1016/j.bsecv.2021.09.007.
[23] J.A. Cebollero, R. Lahoz, M.A. Laguna-Bercero, J.I. Peña, A. Larrea, V.M. Orera, Characterization of laser-processed thin ceramic membranes for electrolyte-supported solid oxide fuel cells, Int. J. Hydrogen Energy. 42 (2017) 13939–13948. https://doi.org/10.1016/j.ijhydene.2016.12.112.
[24] J.A. Cebollero, M.A. Laguna-Bercero, R. Lahoz, J. Silva, R. Moreno, A. Larrea, Optimization of laser-patterned YSZ-LSM composite cathode-electrolyte interfaces for solid oxide fuel cells, J. Eur. Ceram. Soc. 39 (2019) 3466–3474. https://doi.org/10.1016/j.jeurceramsoc.2019.02.049.
[25] G. Cai, Y. Zhang, H. Dai, S. He, L. Ge, H. Chen, L. Guo, Modification of electrode/electrolyte interface by laser micro-processing for solid oxide fuel cell, Mater. Lett. 195 (2017) 232–235. https://doi.org/10.1016/j.matlet.2017.02.095.
[26] L. Zheng, R. Xu, J. Zhang, F. Yu, C. Li, J. Sunarso, W. Zhang, X. Meng, N. Yang, Enhanced electrochemical performance by structural design of electrolyte surface combining 3D printing technology with multi-physical modelling, Chem. Eng. J. 451 (2023) 139038. https://doi.org/10.1016/j.cej.2022.139038.
[27] M.B. Mogensen, Materials for reversible solid oxide cells, Curr. Opin. Electrochem. 21 (2020) 265–273. https://doi.org/10.1016/j.coelec.2020.03.014.
[28] G. Greczynski, L. Hultman, X-ray photoelectron spectroscopy: Towards reliable binding energy referencing, Prog. Mater. Sci. 107 (2020) 100591. https://doi.org/10.1016/j.pmatsci.2019.100591.
[29] X. Majnoni d'Intignano, D. Cademartori, D. Clematis, S. Presto, M. Viviani, R. Botter, A. Barbucci, G. Cerisola, G. Caboche, M.P. Carpanese, Infiltrated Ba0.5Sr0.5Co0.8Fe0.2O3-δ-Based Electrodes as Anodes in Solid Oxide Electrolysis Cells, Energies. 13 (2020) 3659. https://doi.org/10.3390/en13143659.
[30] D. Clematis, T. Ferrari, A. Bertei, A.M. Asensio, M.P. Carpanese, C. Nicolella, A. Barbucci, On the stabilization and extension of the distribution of relaxation times analysis, Electrochim. Acta. 391 (2021) 138916. https://doi.org/10.1016/j.electacta.2021.138916.
[31] L. Cerami, E. Mazur, S. Nolte, C.B. Schaffer, Femtosecond Laser Micromachining, in: Ultrafast Nonlinear Opt., Springer International Publishing, Heidelberg, 2013: pp. 287–321. https://doi.org/10.1007/978-3-319-00017-6_12.
[32] J. Cheng, C. Liu, S. Shang, D. Liu, W. Perrie, G. Dearden, K. Watkins, A review of ultrafast laser materials micromachining, Opt. Laser Technol. 46 (2013) 88–102. https://doi.org/10.1016/j.optlastec.2012.06.037.
[33] J. Cheng, C. Tian, J. Yang, Effects of Fe2O3 addition on the electrical properties of SDC solid electrolyte ceramics, J. Mater. Sci. Mater. Electron. 30 (2019) 16613–16620. https://doi.org/10.1007/s10854-019-02040-2.
[34] A. V. Coles-Aldridge, R.T. Baker, Ionic conductivity in multiply substituted

ceria-based electrolytes, Solid State Ionics. 316 (2018) 9–19. https://doi.org/10.1016/j.ssi.2017.12.013.
[35] M. François, M.P. Carpanese, O. Heintz, V. Lescure, D. Clematis, L. Combemale, F. Demoisson, G. Caboche, Chemical Degradation of the La0.6Sr0.4Co0.2Fe0.8O3−δ/Ce0.8Sm0.2O2−δ Interface during Sintering and Cell Operation, Energies. 14 (2021) 3674. https://doi.org/10.3390/en14123674.
[36] K. Kuntaiah, P. Sudarsanam, B.M. Reddy, A. Vinu, Nanocrystalline Ce1−xSmxO2−δ (x = 0.4) solid solutions: structural characterization versus CO oxidation, RSC Adv. 3 (2013) 7953. https://doi.org/10.1039/c3ra23491f.
[37] H. Idriss, On the wrong assignment of the XPS O1s signal at 531–532 eV attributed to oxygen vacancies in photo- and electro-catalysts for water splitting and other materials applications, Surf. Sci. 712 (2021) 121894. https://doi.org/10.1016/j.susc.2021.121894.
[38] M. Tou, R. Michalsky, A. Steinfeld, Solar-Driven Thermochemical Splitting of CO2 and In Situ Separation of CO and O2 across a Ceria Redox Membrane Reactor, Joule. 1 (2017) 146–154. https://doi.org/10.1016/j.joule.2017.07.015.
[39] P. Kumar, S. Presto, A.S.K. Sinha, S. Varma, M. Viviani, P. Singh, Effect of samarium (Sm3+) doping on structure and electrical conductivity of double perovskite Sr2NiMoO6 as anode material for SOFC, J. Alloys Compd. 725 (2017) 1123–1129. https://doi.org/10.1016/j.jallcom.2017.07.211.
[40] A. Staffolani, A. Baldinelli, G. Bidini, F. Nobili, L. Barelli, Operando Analysis of Losses in Commercial-Sized Solid Oxide Cells: Methodology Development and Validation, Energies. 15 (2022) 4978. https://doi.org/10.3390/en15144978.
[41] J. Hong, A. Bhardwaj, H. Bae, I. Kim, S.-J. Song, Electrochemical Impedance Analysis of SOFC with Transmission Line Model Using Distribution of Relaxation Times (DRT), J. Electrochem. Soc. 167 (2020) 114504. https://doi.org/10.1149/1945-7111/aba00f.
[42] Y. Chen, Y. Bu, Y. Zhang, R. Yan, D. Ding, B. Zhao, S. Yoo, D. Dang, R. Hu, C. Yang, M. Liu, A Highly Efficient and Robust Nanofiber Cathode for Solid Oxide Fuel Cells, Adv. Energy Mater. 7 (2017) 1601890. https://doi.org/10.1002/aenm.201601890.
[43] M.S. Khan, X. Xu, R. Knibbe, Z. Zhu, Air electrodes and related degradation mechanisms in solid oxide electrolysis and reversible solid oxide cells, Renew. Sustain. Energy Rev. 143 (2021) 110918. https://doi.org/10.1016/j.rser.2021.110918.
[44] W. Zhang, Y. Zhou, E. Liu, Y. Ding, Z. Luo, T. Li, N. Kane, B. Zhao, Y. Niu, Y. Liu, M. Liu, A highly efficient and durable air electrode for intermediate-temperature reversible solid oxide cells, Appl. Catal. B Environ. 299 (2021) 120631. https://doi.org/10.1016/j.apcatb.2021.120631.
[45] A. Giuliano, M.P. Carpanese, D. Clematis, M. Boaro, A. Pappacena, F. Deganello, L.F. Liotta, A. Barbucci, Infiltration, Overpotential and Ageing Effects on Cathodes for Solid Oxide Fuel Cells: La 0.6 Sr 0.4 Co 0.2 Fe 0.8 O 3-δ versus Ba 0.5 Sr 0.5 Co 0.8 Fe 0.2 O 3-δ, J. Electrochem. Soc. 164 (2017) F3114–F3122. https://doi.org/10.1149/2.0161710jes.
[46] D. Clematis, A. Barbucci, S. Presto, M. Viviani, M.P. Carpanese, Electrocatalytic activity of perovskite-based cathodes for solid oxide fuel cells, Int. J. Hydrogen Energy. 44 (2019) 6212–6222. https://doi.org/10.1016/j.ijhydene.2019.01.128.
[47] N. Ai, S. He, N. Li, Q. Zhang, W.D.A. Rickard, K. Chen, T. Zhang, S.P. Jiang, Suppressed Sr segregation and performance of directly assembled La0.6Sr0.4Co0.2Fe0.8O3-δ oxygen electrode on Y2O3-ZrO2 electrolyte of solid

oxide electrolysis cells, J. Power Sources. 384 (2018) 125–135. https://doi.org/10.1016/j.jpowsour.2018.02.082.
[48] S. He, Y. Zou, K. Chen, S.P. Jiang, A critical review of key materials and issues in solid oxide cells, Interdiscip. Mater. 2 (2023) 111–136. https://doi.org/10.1002/idm2.12068.
[49] Z. Pan, Q. Liu, Z. Yan, Z. Jiao, L. Bi, S.H. Chan, Z. Zhong, On the delamination of air electrodes of solid oxide electrolysis cells: A mini-review, Electrochem. Commun. 137 (2022) 107267. https://doi.org/10.1016/j.elecom.2022.107267.
[50] R. Davì, G. Carraro, M. Stojkovska, M. Smerieri, L. Savio, M. Lewandowski, J.-J. Gallet, F. Bournel, M. Rocca, L. Vattuone, Graphene growth on Ni (1 1 1) by CO exposure at near ambient pressure, Chem. Phys. Lett. 774 (2021) 138596. https://doi.org/10.1016/j.cplett.2021.138596.